JOURNAL OF SPACECRAFT AND ROCKETS
Vol. 44, No. 3, May–June 2007

Dynamics and Control of Rotating Tethered Satellite Systems

Mischa Kim* and Christopher D. Hall†
Virginia Polytechnic Institute and State University, Blacksburg, Virginia 24061

DOI: 10.2514/1.17065

The control problems of two different configurations of tethered satellite systems for NASA's Submillimeter Probe of the Evolution of Cosmic Structure (SPECS) mission are studied and their control performances are compared. The configuration of main focus is the TetraStar model composed of three controlled spacecraft and three uncontrolled counterweights. This system is compared with a triangular tethered satellite system consisting of three controlled spacecraft. The equations of motion are derived using Lagrange's equations. Several mission scenarios for the SPECS mission considering the operation of an infrared telescope are introduced and asymptotic tracking laws based on Lyapunov control are developed.

Nomenclature

A	=	tether cross-sectional area, mm^2
a	=	tether dissipation parameter, s
$\mathcal{AE}$	=	tether constant, N
D	=	mirror diameter, m
d	=	unstrained tether length, m
E	=	effective Young's modulus, N/mm^2
$\boldsymbol{e}$	=	error vector
$\boldsymbol{e}_f$	=	filter output vector
e_r	=	radial distance error, m
$\boldsymbol{e}_x$	=	unit vector in x direction, 1
e_θ	=	azimuthal error, rad
$\boldsymbol{F}_d$	=	viscous friction coefficient matrix
$\mathcal{F}_\mathcal{I}$	=	inertial reference frame
$\mathcal{F}_\mathcal{P}$	=	prescribed motion reference frame
f	=	tether tension, N
$\boldsymbol{f}$	=	right-hand side of motion equations
$\boldsymbol{G}$	=	gravity force vector
$\boldsymbol{h}$	=	angular momentum, kg · m^2/s^2
k	=	control parameter, 1
L	=	strained length of outer tether, m
l	=	strained length of inner tether, m
$\boldsymbol{M}$	=	mass matrix
m	=	spacecraft mass, kg
$\boldsymbol{N}$	=	vector of coupling forces
$\boldsymbol{Q}^{(e)}$	=	vector of external forces
$\boldsymbol{Q}^{(i)}$	=	vector of internal forces
$\boldsymbol{q}$	=	vector of generalized coordinates
r	=	radial distance coordinate, m
$\boldsymbol{S}$	=	vector of spring forces
t	=	time, s
$\boldsymbol{U}$	=	vector of control forces
$\boldsymbol{V}_m$	=	centripetal-Coriolis force matrix
$\boldsymbol{x}$	=	state vector
$\boldsymbol{Y}$	=	intermediate variable vector
$\boldsymbol{y}$	=	output vector
z	=	height coordinate, m
α, β, γ	=	system parameters
Γ	=	control parameter matrix, 1
δ	=	projected spring force component direction, m
ϵ	=	tether longitudinal strain, 1
ε	=	projected spring force component direction, m^2
ζ	=	projected spring force component direction, m
$\boldsymbol{\eta}$	=	filtered tracking errorlike variable vector
θ	=	azimuthal angle coordinate, rad
λ	=	wavelength, μm
ρ	=	formation geometry angle, rad
τ	=	tensile stress, N/mm^2
$\boldsymbol{\Upsilon}$	=	intermediate variable vector
υ	=	intermediate variable
ϕ	=	velocity filter variable
$\boldsymbol{\chi}$	=	intermediate variable vector
$\boldsymbol{\Psi}$	=	system parameter vector
$\hat{\boldsymbol{\Psi}}$	=	system parameter vector estimate
$\boldsymbol{\Omega}$	=	system regression matrix
$\boldsymbol{\Omega}_d$	=	desired system regression matrix

Subscripts

f	=	final
i	=	ith spacecraft or initial
ij	=	index of tether connecting spacecraft i and j
∘	=	inner spacecraft
•	=	outer spacecraft

Superscripts

d	=	desired
e	=	equilibrium
opt	=	optimal

Introduction

OVER the past three decades, a variety of concepts have been proposed for space exploration using tethered satellite systems (TSS). These concepts include scientific experiments in the microgravity environment, upper atmospheric research, cargo transfer between orbiting bodies, generation of electricity, and deep space observation [1–3]. Numerous missions have already been launched to verify the tethered system concept for space application. The earliest tethered spacecraft missions were conducted during Project Gemini, when the Gemini vehicle and the Agena target vehicle were connected by a tether and rotational experiments were conducted [4]. Important milestones include retrieval of a tether in space (TSS-1, 1992), successful deployment of a 20 km tether in space (SEDS-1, 1993), closed-loop control of a tether deployment (SEDS-2, 1994), and operation of an electrodynamic tether used in both power and thrust mode (PMG, 1993) [5,6]. The idea of interconnecting spacecraft by means of lightweight deployable tethers has been proven to be particularly attractive also for space observations for various reasons. Variable-baseline interferometric observations can

Received 8 April 2005; revision received 30 January 2006; accepted for publication 30 January 2006.

*Ph.D. Candidate, Currently Assistant Professor, Embry-Riddle Aeronautical University, Department of Aerospace Engineering, Prescott, AZ 86301; mischa.kim@erau.edu. Member AIAA.

†Professor, Department of Aerospace and Ocean Engineering; cdhall@vt.edu. Associate Fellow AIAA.

be achieved by a carefully controlled deployment and retrieval procedure of the tethers. In addition, the observational plane can be densely covered by spinning the tethered system. Lastly, the high levels of propellant consumption demanded by separated spacecraft in formation can be significantly reduced by tension or length control of the interconnecting tethers.

In this paper, we present two configurations for a rotating tethered interferometer with three subaperture telescopes. One configuration is a simple triangular TSS, where the three telescopes are connected by three elastic tethers whose unstretched lengths are all equal. The second configuration, called TetraStar [7], includes six additional tethers and three additional masses that serve as counterweights and assist in controlling the rotational motion. For both configurations, we develop scenarios that are representative of a proposed mission [8] and develop control laws to track the desired motion. The purpose of the paper is to present the two configurations, describe the system models and operational scenarios, and compare the performances of the two configurations.

We begin with a discussion of some relevant papers and articles on the dynamics of TSS and adaptive control of mechanical systems. In the subsequent section we present a brief description of the science mission that motivates this study and introduce the two proposed satellite configurations. We then introduce the system models and develop the motion equations. Relative equilibria are identified and mission scenarios are presented, followed by a thorough discussion on control law development. Finally, the performance of the controllers are validated considering the different mission scenarios.

Literature Review

The problem of dynamics and control of tethered satellite formations has attracted considerable attention over the past decade. Of particular interest in the context of this paper are publications by DeCou [9,10], Keshmiri and Misra [11], Wong and Misra [12] and Farquhar [13]. For a thorough literature review we refer to [14].

Nonlinear adaptive control of dynamical systems has emerged as an increasingly important approach to nonlinear controller design in recent years. Major breakthroughs in adaptive output-feedback control were achieved, amongst others, by Marino and Tomei [15,16] whose work triggered a remarkable development in the following years. In [15] the authors managed to remove the structural restriction that the nonlinearities in the output were not allowed to precede the input. A more general class of systems was considered in their companion paper [16], in which the system was not required to be linear with respect to the unknown parameter vector. The latter results were only obtained, however, for set-point regulation problems. In a more recent paper Marino and Tomei extended the results obtained in [15] for a class of systems with time-varying parameters [17]. The paper by Krstić and Kokotović [18] refined the control approaches developed by Marino and Tomei using such concepts as "tuning functions" and "swapping-based" schemes to allow for incorporation of any standard gradient update law. Khalil [19] considered the problem of adaptive output-feedback control of single-input-single-output systems, which can be nonlinearly dependent on the control input. However, only semiglobal stability could be achieved. Furthermore, a priori knowledge of bounds on parameters and on initial conditions was required, and, more important, persistence of system excitation was sufficient for both parameter and tracking error convergence. Loria presented one of the first papers on global output-feedback control for one-degree-of-freedom Euler–Lagrange systems [20]. The control design exploited the properties of hyperbolic functions to define a "nonlinear approximate differentiation filter" to automatically enlarge the domain of attraction. De Queiroz et al. [21] used a similar approach to achieve global stability for general nth-order uncertain systems, and this work is the major reference for the control approach used here.

SPECS Mission Concept

NASA's future Earth and space science missions involve formation flying of multiple coordinated spacecraft. Several space science missions include distributed instruments, large phased arrays of lightweight reflectors, and long variable-baseline space interferometers. An array of collectors and combiner spacecraft will form variable-baseline space interferometers for a variety of science missions such as the Submillimeter Probe of the Evolution of Cosmic Structure (SPECS) [8]. This particular mission concept was initiated by a NASA science team and proposes a 1-km baseline submillimeter interferometer ($\lambda \approx 40$–$500\ \mu$m). It comprises possibly as few as three 3–4-m-diam mirrors and rotates about the primary optical axis collecting (3–0.25 eV) photons, which are then preprocessed by a central beam collector. Because operating such systems in any kind of Earth orbit is not feasible due to extensive fuel consumption and unsatisfactory photon yield, the second Lagrangian point in the sun–Earth system, L_2, was chosen as the operational environment. The SPECS spacecraft formation is intended to be placed in a halo orbit about this libration point [22].

The two tethered satellite configurations we compare in this paper are a triangular system and a more complex formation called TetraStar [7]. The latter system consists of a total of three controlled spacecraft and three uncontrolled counterweights. Figures 1a–1c show a schematic layout of TetraStar during tether deployment. The three inner point masses denote the controlled spacecraft and form what we refer to as the "inner" system; the outer point masses ("outer" system) mark the uncontrolled counterweights. Additionally, the three tethers interconnecting the controllable spacecraft are deployable, whereas the unstrained tether length d for the remaining six tethers is constant. Note that the triangular configuration can be obtained from the TetraStar model by removing the outer point masses and the corresponding tethers.

From a controls point of view, TetraStar offers significant benefits over the triangular TSS. As we showed in an earlier work [14], the overall control effort for a triangular TSS can be divided into two parts. The first and major contribution to the total control impulse is required in the angular direction and regulates the angular momentum of the TSS according to the desired trajectory. The second control part is a radial control component, which significantly contributes to the overall control effort only during times when the TSS is in a transitional phase between steady spin and tether deployment or retrieval and vice versa. The TetraStar model can

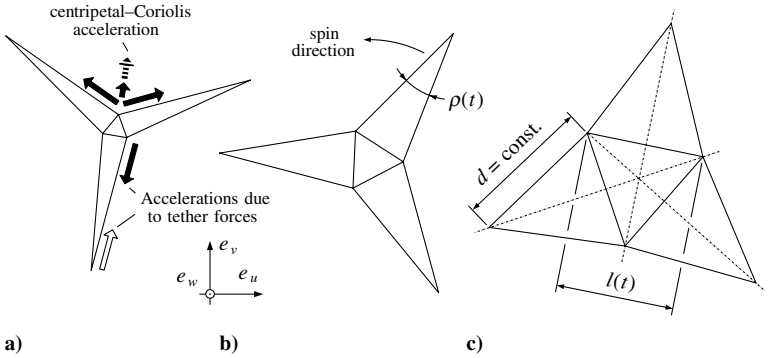

Fig. 1 Deployment of the TetraStar system.

improve the control performance on both counts. First, the three counterweights in combination with the corresponding tethers provide additional control authority in the radial direction for $\rho(t) < \pi/3$. In Fig. 1a these additional force components are identified by full arrows; the broken arrow denotes a centripetal-Coriolis acceleration component. Second and more important, if dimensioned correctly these counterweights can act as a buffer to balance the increase and decrease in angular momentum during tether deployment and retrieval, which is due to the controlled spacecraft.

System Model and Equations of Motion

In this section equations of motions (EOM) of the system are formulated using the system description developed in [23]. The mechanical system considered is shown in Fig. 2 with TetraStar. It is composed of a system of n point masses interconnected arbitrarily by m idealized tethers. The tethers are assumed to be massless and extensible, capable of exerting force only along the straight line connecting the respective masses. Also, the tethers do not support compression or any components of shear forces or bending moments and are therefore assumed to be perfectly flexible. The constitutive character for the tethers is taken as viscoelastic, allowing intrinsic energy dissipation. Because the system is ultimately being operated at the second Lagrangian point L_2 in the sun–Earth system, gravitational and other environmental forces are assumed to be negligible, but are readily incorporated into the model if necessary.

The EOM are derived using Lagrange's equations defined in a "prescribed motion" reference frame $\mathcal{F}_\mathcal{P}$ rather than in an inertial reference frame $\mathcal{F}_\mathcal{I}$. Cylindrical coordinates relative to $\mathcal{F}_\mathcal{P}$ are chosen to describe the position of the point masses. As illustrated in Fig. 2, r_i, θ_i, and z_i are the radial distance in the $\boldsymbol{e}_x\boldsymbol{e}_y$ plane, the angle between the $\boldsymbol{e}_x$ axis and the projection of the position vector $\boldsymbol{q}_i$ onto the $\boldsymbol{e}_x\boldsymbol{e}_y$ plane, and the axial distance in $\boldsymbol{e}_z$ direction of the point mass m_i, respectively. Note that during an observation the TSS rotates in the so-called uv plane, which is defined as the plane perpendicular to the target direction. The motion equations for the controlled system are

$$\boldsymbol{M}_i\ddot{\boldsymbol{q}}_i = \boldsymbol{Q}_i^{(e)} + \boldsymbol{N}_i + \boldsymbol{S}_i + \boldsymbol{U}_i, \qquad i = 1, 2, \ldots, n \tag{1}$$

where

$$\boldsymbol{M}_i = m_i\begin{bmatrix} 1 & 0 & 0 \\ 0 & r_i^2 & 0 \\ 0 & 0 & 1 \end{bmatrix}, \qquad \boldsymbol{q}_i = \begin{pmatrix} r_i \\ \theta_i \\ z_i \end{pmatrix}$$
$$\boldsymbol{Q}_i^{(e)} = \begin{pmatrix} F_{ri} \\ r_i F_{ti} \\ F_{zi} \end{pmatrix}, \qquad \boldsymbol{S}_i = \boldsymbol{Q}_i^{(i)} \tag{2}$$

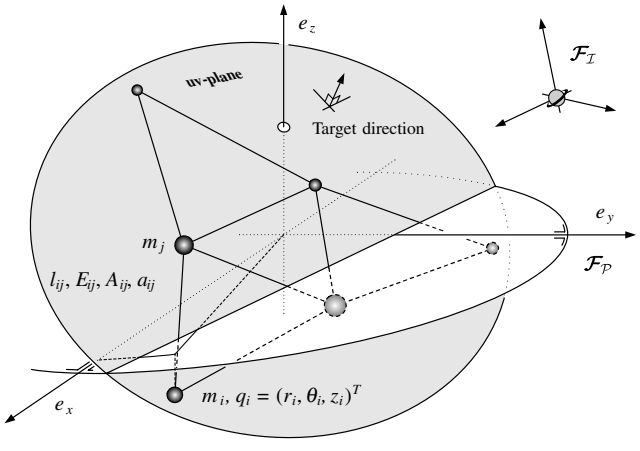

Fig. 2 System model in cylindrical coordinates.

The spring forces in Eqs. (1) are obtained assuming a Kelvin–Voigt constitutive law; that is, the tensile stress τ_{ij} and the longitudinal strain ϵ_{ij} are related by

$$\tau_{ij} = E_{ij}(\epsilon_{ij} + a_{ij}\dot{\epsilon}_{ij}) \qquad i, j = 1, 2, \ldots n \quad \text{and} \quad i \neq j \tag{3}$$

The longitudinal strain in the tether is defined as

$$\epsilon_{ij} = \frac{l_{ij} - d_{ij}}{d_{ij}} \tag{4}$$

Hence, if A_{ij} is the effective cross-sectional area of the tether, then the tension is given by

$$f_{ij} = \begin{cases} A_{ij}\tau_{ij} & \text{if } \epsilon_{ij} \geq 0 \quad \text{and} \quad \tau_{ij} \geq 0 \\ 0 & \text{otherwise} \end{cases} \tag{5}$$

which introduces discontinuities because the tethers do not support compression. Defining the vector of generalized coordinate vectors for the system as

$$\boldsymbol{q} = \left(\boldsymbol{q}_1^T, \boldsymbol{q}_2^T, \ldots, \boldsymbol{q}_{n-1}^T, \boldsymbol{q}_n^T\right)^T \tag{6}$$

Eqs. (1) can be combined to yield

$$\boldsymbol{M}\ddot{\boldsymbol{q}} = \boldsymbol{Q}^{(e)} + \boldsymbol{N} + \boldsymbol{S} + \boldsymbol{U} \tag{7}$$

where

$$\boldsymbol{M} = \begin{bmatrix} \boldsymbol{M}_1 & \boldsymbol{0}_3 & \ldots & \boldsymbol{0}_3 \\ \boldsymbol{0}_3 & \boldsymbol{M}_2 & \ldots & \boldsymbol{0}_3 \\ \vdots & \vdots & \ddots & \vdots \\ \boldsymbol{0}_3 & \boldsymbol{0}_3 & \ldots & \boldsymbol{M}_n \end{bmatrix}, \qquad \boldsymbol{Q}^{(e)} = \begin{pmatrix} \boldsymbol{Q}_1^{(e)} \\ \boldsymbol{Q}_2^{(e)} \\ \vdots \\ \boldsymbol{Q}_n^{(e)} \end{pmatrix}$$
$$\boldsymbol{N} = \begin{pmatrix} \boldsymbol{N}_1 \\ \boldsymbol{N}_2 \\ \vdots \\ \boldsymbol{N}_n \end{pmatrix}, \qquad \boldsymbol{S} = \begin{pmatrix} \boldsymbol{S}_1 \\ \boldsymbol{S}_2 \\ \vdots \\ \boldsymbol{S}_n \end{pmatrix}, \qquad \boldsymbol{U} = \begin{pmatrix} \boldsymbol{U}_1 \\ \boldsymbol{U}_2 \\ \vdots \\ \boldsymbol{U}_n \end{pmatrix} \tag{8}$$

where $\boldsymbol{0}_3$ is the 3×3 null matrix and where the spring forces $\boldsymbol{S}_i$ can be written as

$$\boldsymbol{S}_i = \sum_{\substack{j=1 \\ j\neq i}}^{n=3} \frac{f_{ij}}{l_{ij}}\begin{pmatrix} \delta_{ij} \\ \varepsilon_{ij} \\ \zeta_{ij} \end{pmatrix} \tag{9}$$

introducing the quantities

$$\delta_{ij} = r_j\cos(\theta_j - \theta_i) - r_i \qquad \varepsilon_{ij} = r_i r_j \sin(\theta_j - \theta_i)$$
$$\zeta_{ij} = z_j - z_i \tag{10}$$

Notice that Eqs. (7) are readily integrated after being transformed to a set of $2 \times 3n$ first-order ordinary differential equations (ODEs); that is, defining $\boldsymbol{x} = (\boldsymbol{q}, \dot{\boldsymbol{q}})^T$, Eqs. (7) can be written in compact form as

$$\dot{\boldsymbol{x}} = \boldsymbol{f}(\boldsymbol{x}), \quad \text{where } \boldsymbol{f}(\boldsymbol{x}) = \begin{pmatrix} \dot{\boldsymbol{q}} \\ \boldsymbol{M}^{-1}(\boldsymbol{Q}^{(e)} + \boldsymbol{N} + \boldsymbol{S} + \boldsymbol{U}) \end{pmatrix} \tag{11}$$

For the subsequent analysis we consider two different TSS configurations. The triangular system comprises $n = 3$ point masses and $m = 3$ tethers, whereas the TetraStar system consists of $n = 6$ point masses and $m = 9$ tethers. In any case, we are only interested in symmetrical TSS. That is, for the triangular system all the point masses are equal ($m_i = m$). The same applies to all of the tether parameters. For TetraStar all point masses and tethers belonging to the outer system have similar characteristics, and so do the point masses and tethers of the inner system. For the sake of convenience we introduce the following notation: subscripts $\circ$ and $\bullet$ are used to denote physical quantities such as states and parameters corresponding to the inner and outer system,

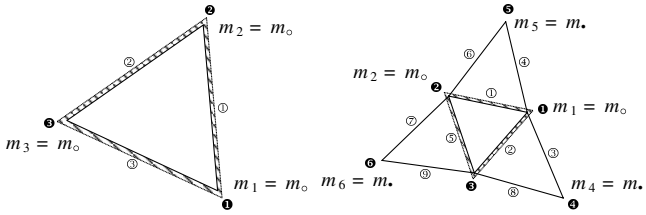

Fig. 3 Labeling of different system configurations.

respectively. For example, for TetraStar,

$$m_i = \begin{cases} m_\circ & \text{for } i = 1,2,3 \\ m_\bullet & \text{for } i = 4,5,6 \end{cases} \tag{12}$$

Figure 3 shows a schematic layout of the labeling of the tethers and point masses for the two satellite configurations. The inner subsystems are marked by a hatched border.

In the following section we identify relative equilibria for the triangular system and for TetraStar.

Relative Equilibria

In the rotating reference frame $\mathcal{F}_\mathcal{P}$ the relative equilibrium motion satisfies

$$\dot{\boldsymbol{x}}^e = \boldsymbol{f}(\boldsymbol{x}^e) = 0 \tag{13}$$

where the superscript denotes the relative equilibrium state. Assuming perfectly symmetrical TSS configurations in the case of the triangular system, it is sufficient to analyze either of the subsystems described by Eqs. (1). For TetraStar two subsystems have to be solved simultaneously, one of which corresponds to an inner point mass. The second subsystem corresponds to one of the two corresponding outer point masses.

Relative Equilibria for a Triangular System

Solving Eq. (13) for $\boldsymbol{x}^e$ we find three conditions for each of the three point masses of the form

$$r_\circ^e = \text{const} \tag{14}$$

$$\dot{\theta}_\circ^e\left(r_\circ^e\right) = \sqrt{\frac{\sqrt{3}\mathcal{A}\mathcal{E}_\circ\left(\sqrt{3}r_\circ^e - d_\circ\right)}{m_\circ r_\circ^e d_\circ}} \qquad \left(\text{note: } l_\circ^e = \sqrt{3}r_\circ^e\right) \tag{15}$$

$$z_\circ^e = \text{const} \tag{16}$$

where we have introduced the variable $\mathcal{A}\mathcal{E}_\circ = A_\circ E_\circ$. Therefore, the relative equilibrium angular velocity for the TSS is

$$\dot{\theta}_\circ^e(l_\circ^e) = \sqrt{\frac{3\mathcal{A}\mathcal{E}_\circ\left(l_\circ^e - d_\circ\right)}{m_\circ l_\circ^e d_\circ}} \tag{17}$$

which shows that the rotating TSS has to be under tension ($l_\circ^e > d_\circ$).

Relative Equilibria for TetraStar

In the case of TetraStar, conditions for a relative equilibrium are obtained effortlessly using d'Alembert's principle or the principle of virtual work.

These conditions are

$$r_\circ^e = \text{const} \tag{18}$$

$$r_\bullet^e = \text{const} \tag{19}$$

$$m_\circ(\dot{\theta}^e)^2 r_\circ^e = \sqrt{3}\frac{\mathcal{A}\mathcal{E}_\circ\left(l_\circ^e - d_\circ^e\right)}{d_\circ^e} - \left(r_\bullet^e - 2r_\circ^e\right)\frac{\mathcal{A}\mathcal{E}_\bullet\left(l_\bullet^e - d_\bullet\right)}{l_\bullet^e d_\bullet}$$
$$l_\bullet^e = \sqrt{r_\circ^{e2} + r_\bullet^{e2} - r_\circ^e r_\bullet^e} \tag{20}$$

$$m_\bullet(\dot{\theta}^e)^2 r_\bullet^e = \left(2r_\bullet^e - r_\circ^e\right)\frac{\mathcal{A}\mathcal{E}_\bullet\left(l_\bullet^e - d_\bullet\right)}{l_\bullet^e d_\bullet} \tag{21}$$

$$z_\circ^e = z_\bullet^e = \text{const} \tag{22}$$

Note that for the symmetrical TetraStar system $\dot{\theta}_\circ^e = \dot{\theta}_\bullet^e \equiv \dot{\theta}^e$, Eq. (21) can be rewritten to yield a quartic equation in $r_\bullet^e$ of the following form:

$$\left(r_\bullet^e\right)^4 + \left(r_\bullet^e\right)^3 r_\circ^e\left(\frac{2\beta}{\alpha} - 1\right) + \left(r_\bullet^e\right)^2\left\{r_\circ^{e2}\left(\frac{\beta}{\alpha} - 1\right)^2 - \left(\frac{2\gamma}{\alpha}\right)^2\right\}$$
$$+ r_\bullet^e\left\{\left(r_\circ^e\right)^3\frac{\beta}{\alpha}\left(2 - \frac{\beta}{\alpha}\right) + r_\circ^e\left(\frac{2\gamma}{\alpha}\right)^2\right\}$$
$$+ \left(r_\circ^e\right)^2\left\{\left(r_\circ^e\right)^2\left(\frac{\beta}{\alpha}\right)^2 - \left(\frac{\gamma}{\alpha}\right)^2\right\} = 0 \tag{23}$$

where

$$\alpha = m_\bullet(\dot{\theta}^e)^2 d_\bullet - 2\mathcal{A}\mathcal{E}_\bullet, \qquad \beta = \mathcal{A}\mathcal{E}_\bullet, \qquad \gamma = \mathcal{A}\mathcal{E}_\bullet d_\bullet \tag{24}$$

For known tether parameters and a given fixed length of the outer tethers $d_\bullet$, Eq. (23) can be solved for $r_\bullet^e$ in terms of $r_\circ^e$ using a Newton–Raphson method. Equations (20) and (21) can then be used to solve for the only remaining unknown: the unstretched tether length of the inner tethers $d_\circ^e$, which yields

$$d_\circ^e = r_\circ^e\frac{3\mathcal{A}\mathcal{E}_\circ}{(\dot{\theta}^e)^2\left\{m_\circ r_\circ^e + m_\bullet r_\bullet^e\left[\left(r_\bullet^e - 2r_\circ^e\right)/\left(2r_\bullet^e - r_\circ^e\right)\right]\right\} + \sqrt{3}\mathcal{A}\mathcal{E}_\circ} \tag{25}$$

Note that in the limit as $\mathcal{A}\mathcal{E}_\circ \to \infty$ (extremely stiff tethers, rigid TSS), $d_\circ^e \to l_\circ^e = \sqrt{3}r_\circ^e$, as expected.

Figures 4 and 5 show typical uncontrolled initial conditions perturbation responses for the triangular system and for TetraStar for system parameters listed in Table 1. Unperturbed initial conditions result in relative equilibrium motion. Additionally, in Fig. 5 we show the effect of tether damping for $a_{ij} = 0.5$ s. Comparing the two system responses, we point out that coordinate errors measured relative to the unperturbed system motions are notably greater for TetraStar, especially in the angular direction. The system response signals can be thought of as a superposition of three signal components that are best explained with the upper two plots of Fig. 5. The high-frequency oscillations reflect tether vibrations, which can be significantly reduced by increasing the dissipation parameters a_{ij}. Notice that the radial error signal for the counterweight carries an additional high-frequency signal component compared to the inner point mass, which results from increased tether stiffness of the outer tethers (see Table 1). The signal component with a time period of approximately 95 s is due to the rotation of the TSS. The signal amplitudes are increasing because the choice of initial conditions results in a nonzero system linear momentum. The set of initial conditions perturbations chosen for TetraStar yields a relatively decreased system angular momentum; hence the TSS rotates notably slower than the unperturbed satellite formation.

Mission Scenarios for SPECS

This section briefly discusses two mission scenarios to validate the control law developed in the following section. For a detailed

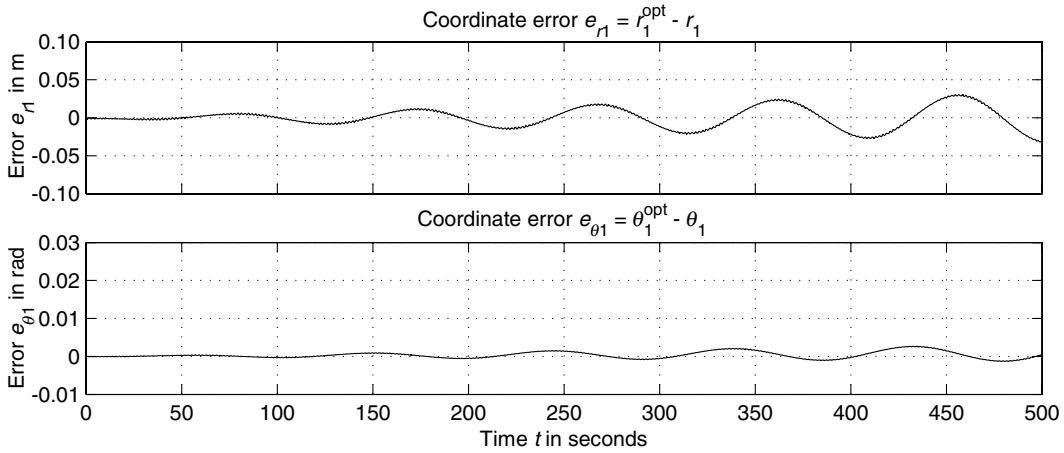

Fig. 4 Triangle: uncontrolled initial conditions perturbation response. The output error is measured relative to a relative equilibrium motion.

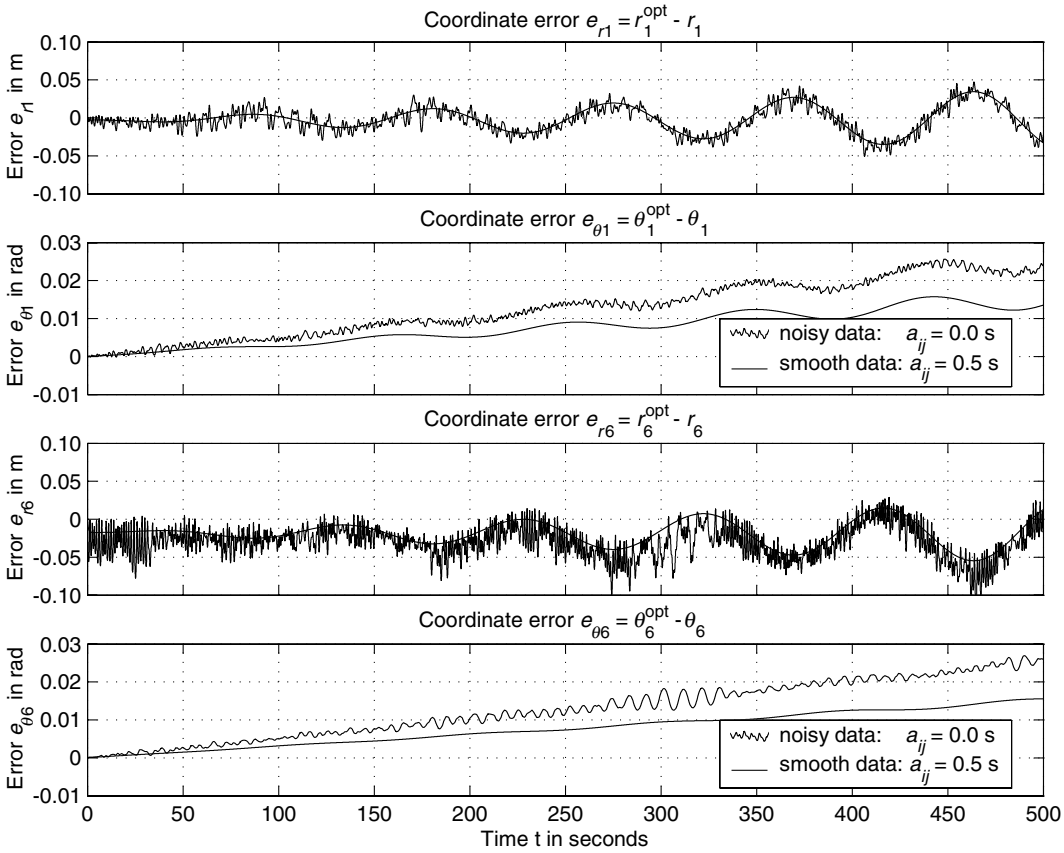

Fig. 5 TetraStar: uncontrolled initial conditions perturbation response. The output error is measured relative to a relative equilibrium motion. Damping ($a_{ij} > 0$) reduces high-frequency oscillations.

Table 1 System and simulation parameters

Parameter	Value
Point masses $m_\circ$, kg	50.0
Point masses $m_\bullet$, kg	5.644
Young's moduli $E_\circ$, N/mm^2	10,000
Young's moduli $E_\bullet$, N/mm^2	15,000
Tether cross sections $A_\circ$, mm^2	1.0
Tether cross sections $A_\bullet$, mm^2	1.0
Damping parameters $a_\circ$, s	0.0
Damping parameters $a_\bullet$, s	0.0
Mirror diameters D_i, m	3.0
Unstretched tether length $d_\bullet$, m	65.0
Initial radial distance R_0, m	15.0
Final radial distance R_f, m	35.0
Integration time step dt, s	0.01
IC disturbances $\delta x_{i,j}$, in $[\delta x_{i,j}]$	10^{-3}

analysis we refer to [14]. The first mission scenario considers the stabilization of a particular relative equilibrium motion of the TSS. This case is of importance for those phases during the sequence of observations when the satellite formation needs to be reoriented to point at specific targets of interest. The second mission scenario represents a SPECS relevant trajectory including a tether deployment and retrieval procedure, which allows the system to densely cover the observational plane in an optimal fashion. For this particular scenario an additional scientifically motivated constraint is formulated, which requires that the instantaneous tangential velocity of the controlled point masses never exceeds a maximum value.

In [14] we commented on the importance of implementing "smooth" mission trajectories to minimize the required control input, and we introduced smoothing functions for those critical periods of time when the TSS is in a transitional phase between a relative equilibrium motion and a tether deployment or retrieval process.

Up to this point the outer point masses have not entered the analysis. As mentioned before, their purpose is to provide additional control authority in the radial direction and serve as a buffer for the system angular momentum during tether deployment and retrieval. To use the interferometer efficiently we require the instantaneous tangential velocity of the point masses to be equal to the maximum allowable velocity. However, we also require the outer tethers to be of fixed (unstrained) length, which leaves the outer point masses as the only free parameters to work with to obtain increased control performance compared to the triangular TSS. Note that these constraints do not allow an optimal solution to the problem of deploying and retrieving the TSS such that the system angular momentum $\boldsymbol{h}(t) = \text{const}$. However, we can size the outer point masses such that $\boldsymbol{h}(t_i) = \boldsymbol{h}(t_f)$, where t_i and t_f are the initial and final times for tether deployment or retrieval. It is straightforward to show that

$$\boldsymbol{h}(t_i) = \boldsymbol{h}(t_f) \Leftrightarrow m_\circ(r_\circ^i - r_\circ^f) + m_\bullet\left(\frac{\left(r_\bullet^i\right)^2}{r_\circ^i} - \frac{\left(r_\bullet^f\right)^2}{r_\circ^f}\right) = 0 \quad (26)$$

Note that Eq. (26) contains three unknowns, namely, $m_\bullet$, $r_\bullet^i$, and $r_\bullet^f$. Evaluating Eq. (23) at $t = t_i$ and $t = t_f$ adds two more equations, and the resulting system of equations can be solved using a Newton–Raphson method. For the system parameters listed in Table 1 and an unstretched and constant tether length of the outer tethers of $d_\bullet = 65.0$ m, we obtain an outer point mass of $m_\bullet = 5.64$ kg.

Applying the outlined methodology to a realistic 1-km baselength TSS with inner system point masses of $m_\circ = 500$ kg, and an unstretched outer tether length of $d_\bullet = 1100$ m, results in counterweights of $m_\bullet = 3.56$ kg for a full aperture scan.

In the next section the tools necessary to develop a nonlinear adaptive output-feedback controller are introduced.

Control Law Development

A drawback of the observer-based control approach as used by the authors in an earlier paper is that an accurate physical model of the dynamical system is required to guarantee asymptotic stability. Although the mathematical structure of the system is usually well defined, the physical parameters are often not precisely known. Additionally, the cost of implementing a controller based on input-state feedback typically includes the cost of motion sensors, which in turn results in elevated sensor count. Adaptive output-feedback controllers using a velocity-generated filter and an estimator for system parameters offer an elegant solution to the problem.

For this analysis the positions of the inner point masses m_i are chosen as outputs; that is, $\boldsymbol{y}_i \equiv \boldsymbol{q}_i = (r_i, \theta_i, z_i)^T$, $i = 1, 2, 3$. Also, due to the particular choice of control inputs in Eqs. (1), one can show that the triangular system is feedback-linearizable and therefore completely controllable [14]. TetraStar, on the other hand, is clearly uncontrollable due to a lack of control authority (outer system). However, we will show that for the mission scenarios described in the preceding section, the control of the inner system is sufficient. With these results we derive an adaptive output-feedback control law based on the work developed in [21].

Problem Statement

Motivated by the subsequent analysis, we rewrite the motion Eqs. (7) in the following form:

$$\boldsymbol{\Omega}(\boldsymbol{q}, \dot{\boldsymbol{q}}, \ddot{\boldsymbol{q}})\boldsymbol{\Psi} \triangleq \boldsymbol{M}(\boldsymbol{q})\ddot{\boldsymbol{q}} + \boldsymbol{V}_m(\boldsymbol{q}, \dot{\boldsymbol{q}})\dot{\boldsymbol{q}} + \boldsymbol{G}(\boldsymbol{q}) + \boldsymbol{F}_d\dot{\boldsymbol{q}} = \boldsymbol{U} \quad (27)$$

to collect and reorder corresponding terms in $\boldsymbol{q}$, $\dot{\boldsymbol{q}}$, and $\ddot{\boldsymbol{q}}$. We have used the fact that the dynamics equations are linearly parameterizable to define the product $\boldsymbol{\Omega}(\boldsymbol{q}, \dot{\boldsymbol{q}}, \ddot{\boldsymbol{q}})\boldsymbol{\Psi}$, where $\boldsymbol{\Omega}(\boldsymbol{q}, \dot{\boldsymbol{q}}, \ddot{\boldsymbol{q}})$ is the system regression matrix, which contains known functions of $\boldsymbol{q}$, $\dot{\boldsymbol{q}}$, and $\ddot{\boldsymbol{q}}$.

The primary control objective is to design the control input $\boldsymbol{U}$ such that the tracking error vector $\boldsymbol{e} = \boldsymbol{y}^d - \boldsymbol{y} \to 0$ as $t \to \infty$, while the state remains bounded and with the constraint that only position measurements are available. Note that for both TSS under consideration only the inner point masses are controlled, thus we define

$$\boldsymbol{e} = (\boldsymbol{e}_1, \boldsymbol{e}_2, \boldsymbol{e}_3)^T, \quad \text{where } \boldsymbol{e}_i = \boldsymbol{y}_i^d - \boldsymbol{y}_i, \quad i = 1, 2, 3 \quad (28)$$

Filter and Controller Design

To aid the control design and analysis of this section, we define the functions $\tanh\boldsymbol{\xi} \triangleq (\tanh\xi_1, \ldots, \tanh\xi_n)^T$ and $\cosh(\boldsymbol{\xi}) \triangleq \text{diag}\{\cosh\xi_1, \ldots, \cosh\xi_n\}$ for $\boldsymbol{\xi} \in \mathbb{R}^n$. The filtered tracking errorlike variable $\boldsymbol{\eta}$ is then defined as

$$\boldsymbol{\eta} = \dot{\boldsymbol{e}} + \tanh\boldsymbol{e} + \tanh\boldsymbol{e}_f \quad (29)$$

where we introduce the filter output $\boldsymbol{e}_f$, which is defined to have the following dynamics:

$$\dot{\boldsymbol{e}}_f = -\tanh\boldsymbol{e}_f + \tanh\boldsymbol{e} - k\cosh^2(\boldsymbol{e}_f)\boldsymbol{\eta}, \quad \text{with } \boldsymbol{e}_f(0) = \boldsymbol{0} \quad (30)$$

and where k is a positive control gain. To obtain the open-loop dynamics in terms of the filtered tracking errorlike variable, we differentiate Eqs. (29) with respect to time and premultiply the resulting expression by $\boldsymbol{M}(\boldsymbol{q})$ to obtain

$$\begin{aligned}\boldsymbol{M}(\boldsymbol{q})\dot{\boldsymbol{\eta}} = {} & \boldsymbol{M}(\boldsymbol{q})\ddot{\boldsymbol{q}}^d + \boldsymbol{M}(\boldsymbol{q})[\cosh^2(\boldsymbol{e})]^{-1}(\boldsymbol{\eta} - \tanh\boldsymbol{e} - \tanh\boldsymbol{e}_f) \\ & - \boldsymbol{M}(\boldsymbol{q})\ddot{\boldsymbol{q}} + \boldsymbol{M}(\boldsymbol{q})[\cosh^2(\boldsymbol{e}_f)]^{-1} \\ & \times [\tanh\boldsymbol{e} - \tanh\boldsymbol{e}_f - k\cosh^2(\boldsymbol{e}_f)\boldsymbol{\eta}] \end{aligned} \quad (31)$$

where we have used Eqs. (29) and (30). Next we use Eq. (27) to substitute for the term $-\boldsymbol{M}(\boldsymbol{q})\ddot{\boldsymbol{q}}$, which contains time derivatives of the unmeasurable velocity vector. The centripetal-Coriolis term can be expanded into

$$\boldsymbol{V}_m(\boldsymbol{q}, \dot{\boldsymbol{q}})\dot{\boldsymbol{q}} = \boldsymbol{V}_m(\boldsymbol{q}, \dot{\boldsymbol{q}})(\dot{\boldsymbol{q}}^d + \tanh\boldsymbol{e} + \tanh\boldsymbol{e}_f - \dot{\boldsymbol{e}} - \tanh\boldsymbol{e} - \tanh\boldsymbol{e}_f) \quad (32)$$

$$= -\boldsymbol{V}_m(\boldsymbol{q}, \dot{\boldsymbol{q}})(\dot{\boldsymbol{e}} + \tanh\boldsymbol{e} + \tanh\boldsymbol{e}_f) \quad (33)$$

$$+ \boldsymbol{V}_m(\boldsymbol{q}, \dot{\boldsymbol{q}}^d + \tanh\boldsymbol{e} + \tanh\boldsymbol{e}_f)(\dot{\boldsymbol{q}} - \dot{\boldsymbol{q}}^d) \quad (34)$$

$$+ \boldsymbol{V}_m(\boldsymbol{q}, \dot{\boldsymbol{q}}^d)(\dot{\boldsymbol{q}}^d + \tanh\boldsymbol{e} + \tanh\boldsymbol{e}_f) \quad (35)$$

$$= -\boldsymbol{V}_m(\boldsymbol{q}, \dot{\boldsymbol{q}})\boldsymbol{\eta} + \boldsymbol{\Upsilon}(\boldsymbol{q}, \dot{\boldsymbol{q}}^d, \boldsymbol{\eta}, \tanh\boldsymbol{e}, \tanh\boldsymbol{e}_f) + \boldsymbol{V}_m(\boldsymbol{q}, \dot{\boldsymbol{q}}^d)\dot{\boldsymbol{q}}^d \quad (36)$$

where we have used the symmetry property $\boldsymbol{V}_m(\boldsymbol{q}, \boldsymbol{\xi})\boldsymbol{\zeta} = \boldsymbol{V}_m(\boldsymbol{q}, \boldsymbol{\zeta})\boldsymbol{\xi}$ [24], repeatedly. The open-loop dynamics (31) then yields

$$\boldsymbol{M}(\boldsymbol{q})\dot{\boldsymbol{\eta}} = -\boldsymbol{V}_m(\boldsymbol{q}, \dot{\boldsymbol{q}})\boldsymbol{\eta} - k\boldsymbol{M}(\boldsymbol{q})\boldsymbol{\eta} + \boldsymbol{\Omega}_d\boldsymbol{\Psi} + \boldsymbol{\chi} + \tilde{\boldsymbol{Y}} - \boldsymbol{U} \quad (37)$$

where $\boldsymbol{\chi}(\boldsymbol{q}, \dot{\boldsymbol{q}}^d, \boldsymbol{\eta}, \tanh\boldsymbol{e}, \tanh\boldsymbol{e}_f)$ and $\tilde{\boldsymbol{Y}}(\boldsymbol{q}, \boldsymbol{q}^d, \dot{\boldsymbol{q}}^d, \ddot{\boldsymbol{q}}^d)$ are introduced as

$$\begin{aligned}\boldsymbol{\chi} = {} & \boldsymbol{M}(\boldsymbol{q})\{[\cosh^2(\boldsymbol{e})]^{-1}(\boldsymbol{\eta} - \tanh\boldsymbol{e} - \tanh\boldsymbol{e}_f) \\ & + [\cosh^2(\boldsymbol{e}_f)]^{-1}(\tanh\boldsymbol{e} - \tanh\boldsymbol{e}_f)\} \\ & + \boldsymbol{\Upsilon}(\boldsymbol{q}, \dot{\boldsymbol{q}}^d, \boldsymbol{\eta}, \tanh\boldsymbol{e}, \tanh\boldsymbol{e}_f) \end{aligned} \quad (38)$$

and

$$\tilde{\boldsymbol{Y}} = \boldsymbol{M}(\boldsymbol{q})\ddot{\boldsymbol{q}}^d + \boldsymbol{V}_m(\boldsymbol{q}, \dot{\boldsymbol{q}}^d)\dot{\boldsymbol{q}}^d + \boldsymbol{G}(\boldsymbol{q}) + \boldsymbol{F}_d\dot{\boldsymbol{q}} - \boldsymbol{\Omega}_d\boldsymbol{\Psi} \tag{39}$$

In Eqs. (37) and (39) we have introduced the desired regression matrix $\boldsymbol{\Omega}_d$, which is obtained from $\boldsymbol{\Omega}$ by exchanging $\boldsymbol{q}^{(i)} \leftrightarrow (\boldsymbol{q}^d)^{(i)}$, $i = 0, 1, 2$. Note that the desired regression matrix plays the role of the desired trajectory when using input-state feedback linearization, for instance. For the open-loop dynamics described by Eq. (41), it is proven in [21] that the following control input yields asymptotic stability:

$$\boldsymbol{U} = \boldsymbol{\Omega}_d\hat{\boldsymbol{\Psi}} - k\cosh^2(\boldsymbol{e}_f)\tanh\boldsymbol{e}_f + \tanh\boldsymbol{e} \tag{40}$$

where the parameter estimate vector $\hat{\boldsymbol{\Psi}}$ is generated according to a gradient update law

$$\dot{\hat{\boldsymbol{\Psi}}} = \Gamma\boldsymbol{\Omega}_d^T\boldsymbol{\eta}, \quad \text{with } \Gamma = \Gamma^T > 0 \tag{41}$$

Note that the control input in Eqs. (40) requires the computation of $\boldsymbol{e}_f$ (or rather $\boldsymbol{\eta}$) and therefore $\dot{\boldsymbol{e}}$. To obtain a control law with only position measurements, define $\boldsymbol{\upsilon} = \upsilon_i \triangleq \tanh\boldsymbol{e}_f$ and notice that

$$\dot{\upsilon}_i = \frac{\dot{e}_{fi}}{\cosh^2(e_{fi})} = \left(\upsilon_i^2 - 1\right)(\upsilon_i - \tanh e_i) - k(\dot{e}_i + \tanh e_i + \upsilon_i), \quad \text{with } \upsilon_i(0) = 0 \tag{42}$$

which can be rewritten as follows:

$$\dot{\phi}_i = \{(\phi_i - ke_i)^2 - 1\}(\phi_i - ke_i - \tanh e_i) - k(\tanh e_i + \phi_i - ke_i) \tag{43}$$

using $\upsilon_i = \phi_i - ke_i$ and where $\phi_i(0) = ke_i(0)$. With the help of Eq. (43), $\boldsymbol{\upsilon}$ and therefore $\tanh\boldsymbol{e}_f$ can be calculated with position measurements only. Using filter (43) the parameter update law can be integrated with respect to time to yield

$$\hat{\boldsymbol{\Psi}} = \Gamma\boldsymbol{\Omega}_d^T\boldsymbol{e} + \Gamma\int_0^t \left\{\boldsymbol{\Omega}_d^T(\tanh\boldsymbol{e} + \boldsymbol{\upsilon}) - \dot{\boldsymbol{\Omega}}_d^T\boldsymbol{e}\right\} \mathrm{d}\tau \tag{44}$$

where we have used definition (29) and integrated by parts to replace the term containing time derivatives of the error vector, namely, $\dot{\boldsymbol{e}}$. Finally, the control law (40) can be written componentwise:

$$U_i = (\boldsymbol{\Omega}_d\hat{\boldsymbol{\Psi}})_i - \frac{k\upsilon_i}{1 - \upsilon_i^2} + \tanh e_i \tag{45}$$

Equations (43–45) represent the velocity filter, the parameter estimator, and the control law, respectively. Note that the controller (45) has the same basic structure as a conventional controller based on input-state feedback linearization. The first term is a feedforward term, which contains the desired system dynamics and for $\boldsymbol{e} = \dot{\boldsymbol{e}} = \boldsymbol{0}$ exactly cancels the right-hand side of the motion equations. The second and third term regulate the velocitylike and the position error vectors, respectively.

Examples

We developed and implemented a generic simulation code in C++ to validate the performance of the control laws presented in the preceding sections. In particular, the mission scenarios described earlier were used to define desired trajectories. System and simulation parameters are listed in Table 1.

For the perturbed initial conditions response simulation, the perturbation vectors were generated randomly with an upper bound of $\delta x \leq 10^{-3}$ for each element of the vectors. The initial and final

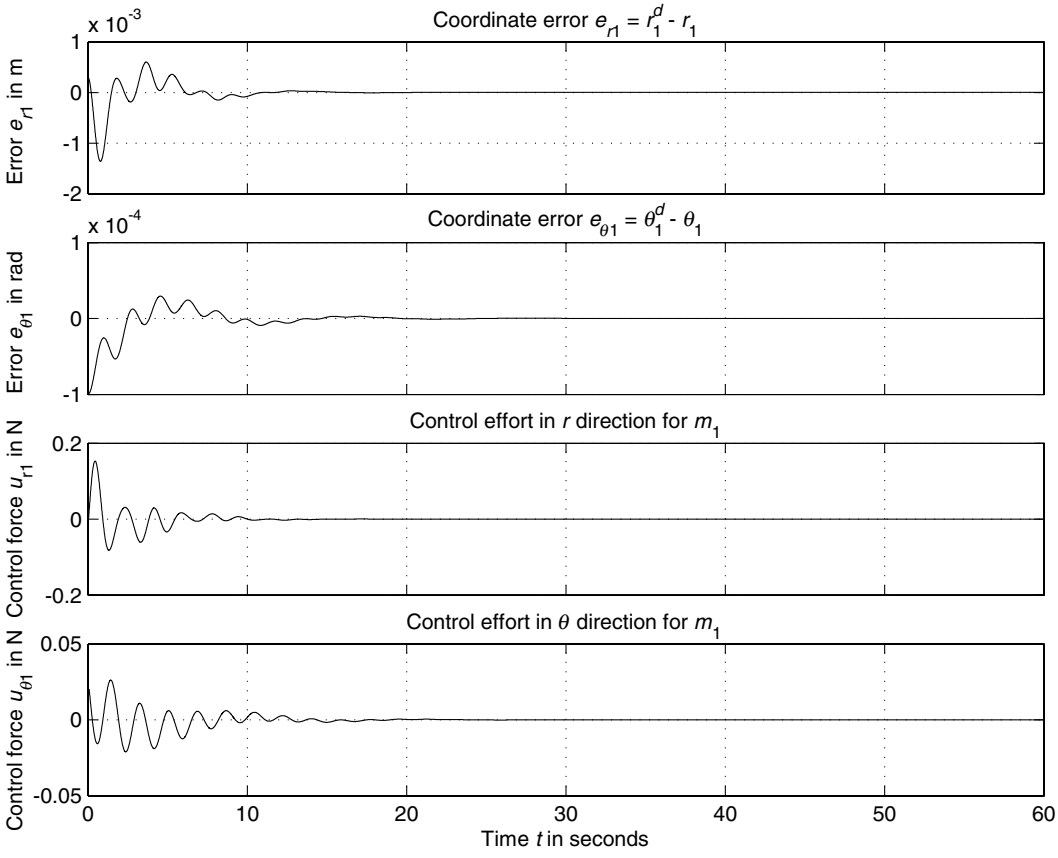

Fig. 6 Triangle: output error and control vector history for an initial conditions perturbation response. The controlled system performs a relative equilibrium motion.

radial distance of the point masses for mission scenario 2 were chosen to be $R_0 = r_{0_+} = 15$ m and $R_f = r_{0_-} = 35$ m. Note that we chose the outer tether length $d_\bullet$ such that the angle between two corresponding outer tethers is $\rho(t) < \pi/3$ (Fig. 1) at all times; hence the additional radial force component due to the outer tethers can assist in the deployment and control process even when the system is fully deployed.

Control parameters for all simulations were tuned to yield comparable control performance in terms of control effort and output error for the triangular system and TetraStar. In particular, the control parameters were chosen as $k = 40.0$ and $\Gamma = \text{diag}\{1, 1, 1, 5, \ldots, 5\}$, where Γ is of proper dimension.

Figures 6–13 show simulation results for the mission scenarios introduced in a preceding section. The initial conditions perturbation responses are illustrated in Figs. 6 and 7 for the triangular system and in Fig. 8 for TetraStar. Comparing Figs. 6 and 8 the triangular system converges considerably faster towards "steady-state" conditions than TetraStar. The controllability of the former system on the one hand and the increased number of parameters to be estimated for the more complex TetraStar configuration on the other hand are the crucial factors resulting in an increase in overall required control input. Note that the parameter estimates for m_i and $\mathcal{AE}_i$, $i = 1, 2, 3$ in Fig. 7 reach steady states that are, however, notably different from the actual parameter values. According to [21], the difference in estimated and actual parameters is not uncommon for mechanical systems and lies in the fact that the primary goal of the controller is to track a desired output and not to accurately estimate the unknown parameter vector.

The results for the SPECS relevant mission scenarios are shown in Figs. 9–13, Figs. 9–11 illustrate the corresponding trajectories.

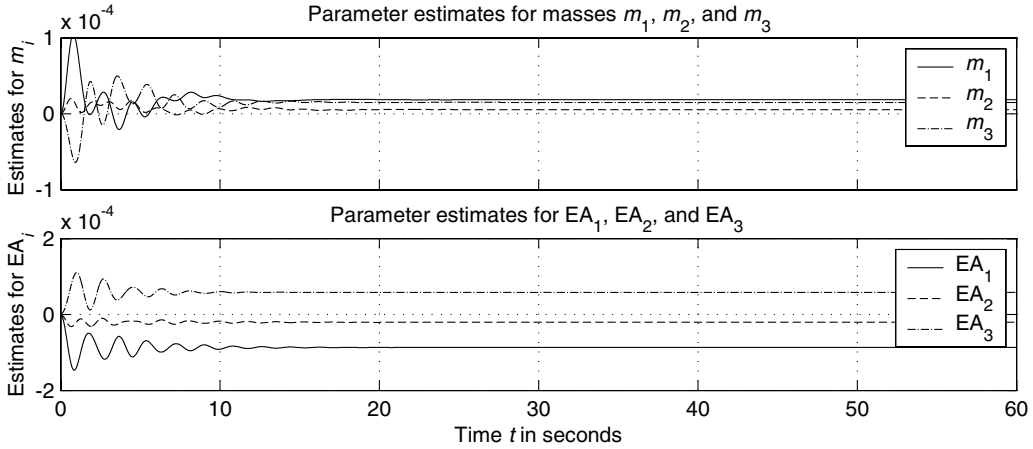

Fig. 7 Triangle: parameter estimate history for a relative equilibrium motion.

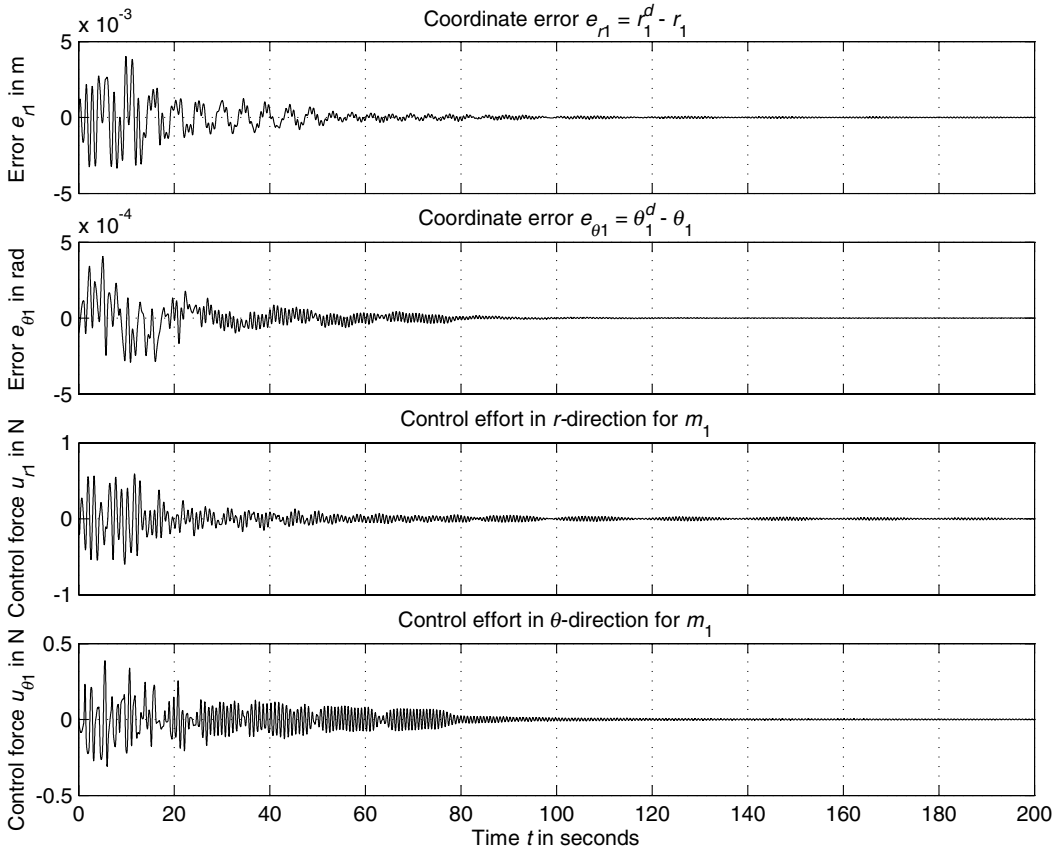

Fig. 8 TetraStar: output error and control vector history for an initial conditions perturbation response. The controlled system performs a relative equilibrium motion.

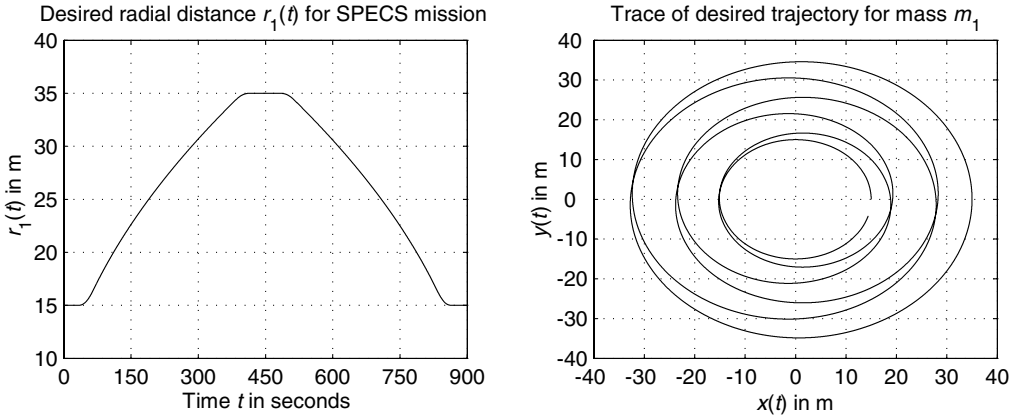

Fig. 9 Triangle: trajectory of point mass m_1 for SPECS relevant mission scenario.

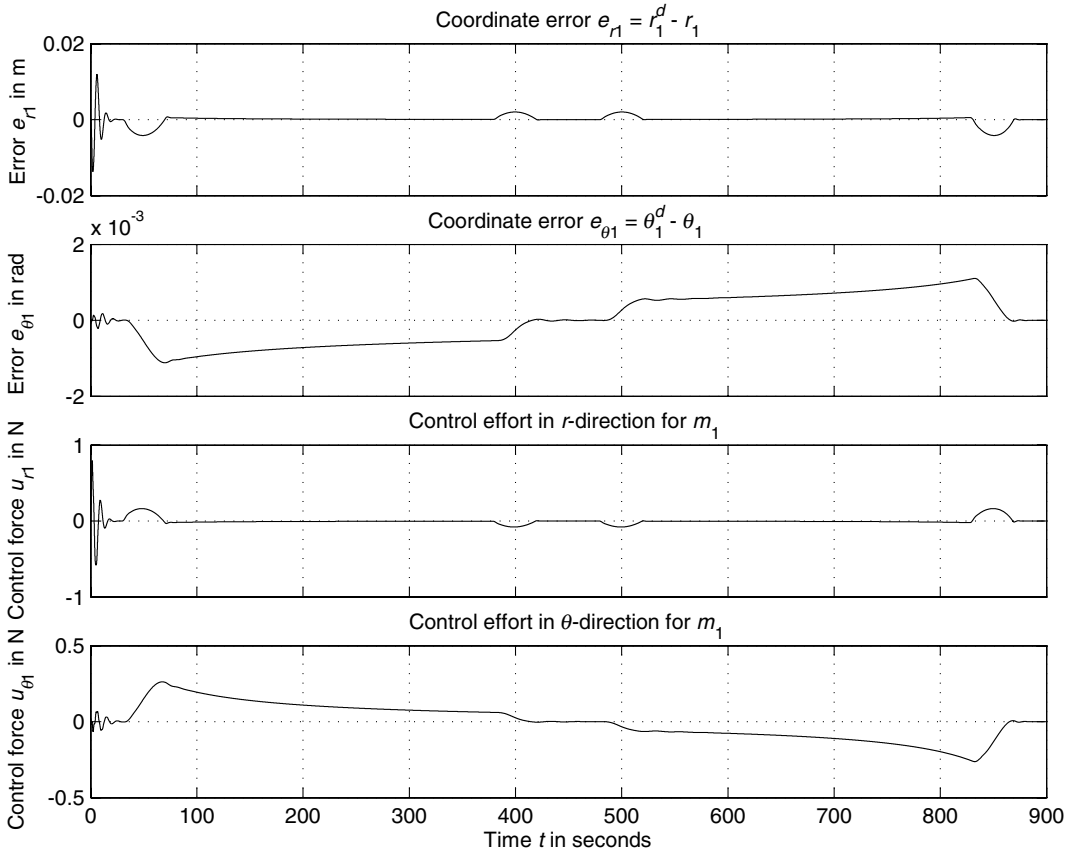

Fig. 10 Triangle: output error and control vector history for SPECS relevant mission scenario.

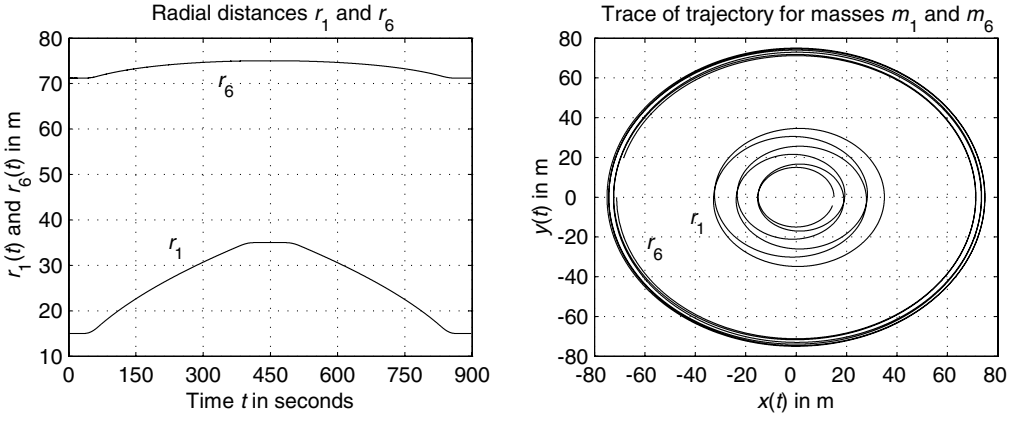

Fig. 11 TetraStar: trajectories of point masses m_1 and m_6 for SPECS relevant mission scenario.

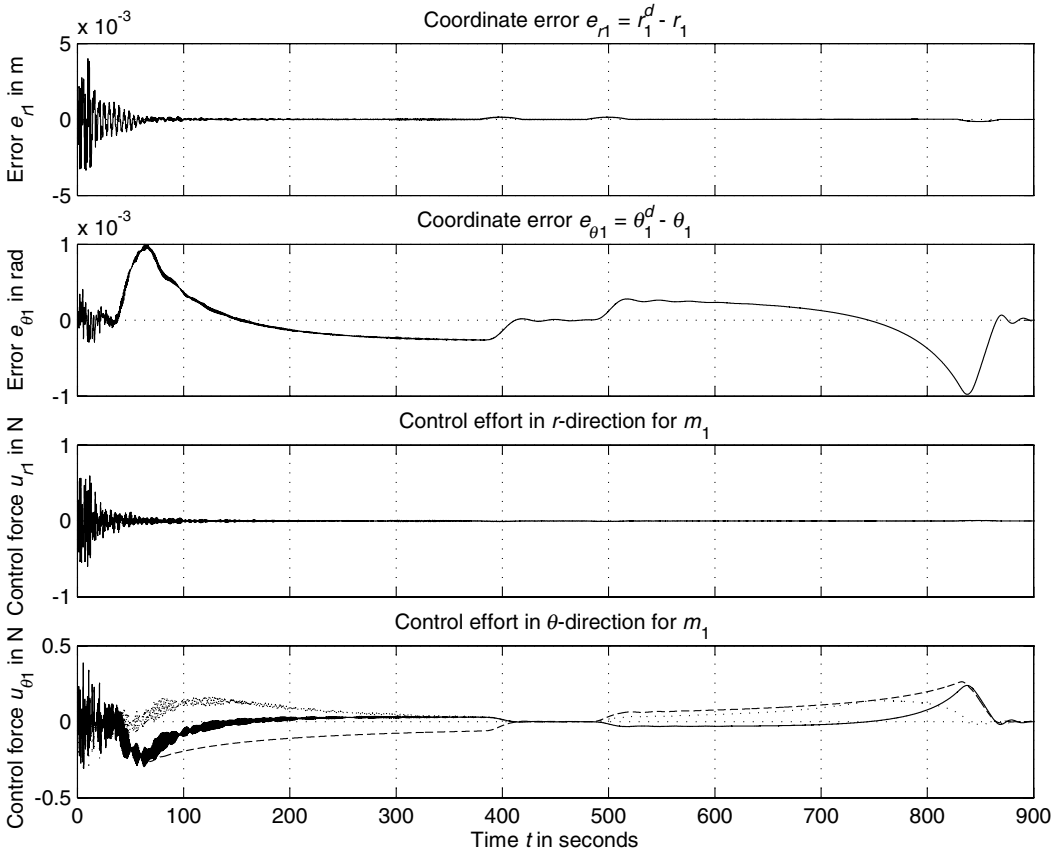

Fig. 12 TetraStar: output error and control vector history for SPECS relevant mission scenario. The graph on the bottom compares the negative (for better visual comparison) angular control efforts of the triangular system (dashed line) and TetraStar (solid line), and shows the difference between the two (dotted line).

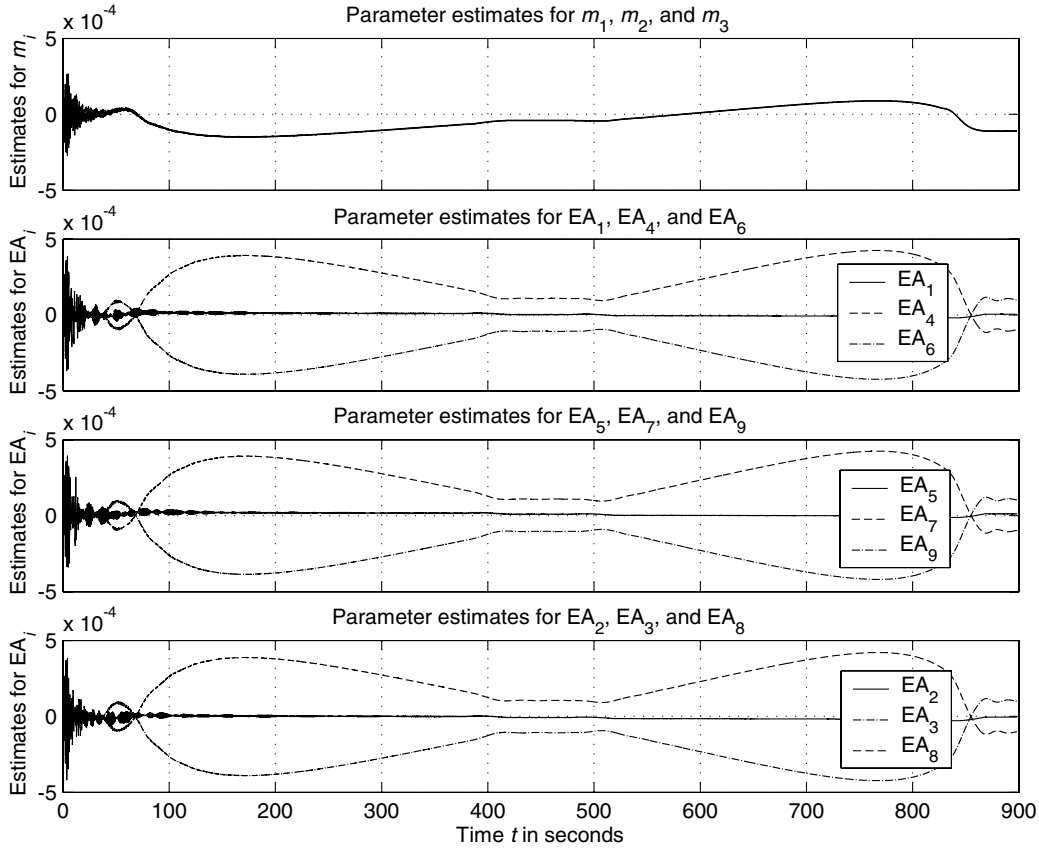

Fig. 13 TetraStar: parameter estimate history for SPECS relevant mission scenario.

Similar to the previous simulation results, the triangular systems converge rapidly towards an "optimal" control state lacking high-frequency oscillations. Both control input and signal error are comparable in magnitude for both satellite formations; however, we observe a significant decrease in required control effort in radial and angular direction in the case of TetraStar. The bumps in the radial control signal shown in Fig. 10 have disappeared in Fig. 12 due to the additional radial force component of the outer tethers. More important, the control effort in the angular direction is significantly reduced for TetraStar, as shown in Fig. 12. The corresponding (negative, for better comparison) control effort for the triangular system is shown here for comparison (dashed line). For this particular simulation we obtain a decrease in overall required control effort for TetraStar of about 75%, about 68% in angular direction. We point out, however, that the particular strategy of choosing the outer point masses following the approach developed in a preceding section might not yield an optimal solution to the problem. Especially for large final baselengths with a ratio of $r_\circ^f / r_\circ^i \approx 40.0$, TetraStar shows significant benefits when the outer tethers are allowed to be deployable, as preliminary simulation results show. Figure 13 shows the parameter estimate history for the SPECS relevant mission scenario for TetraStar. Other than for mission scenario 1, the parameters are not approaching final constant values but show a cyclic symmetry owing to the symmetry of the TetraStar configuration. The time dependence of the parameter vector comes as no surprise because for the SPECS relevant mission scenario we introduced explicit time dependence in the motion equations during tether deployment and retrieval.

Conclusions

Techniques to control the motion of TSS composed of n point masses and interconnected by m idealized tethers are presented. Specifically, the control problems of a triangular TSS and a satellite configuration called TetraStar are discussed. Mission scenarios for NASA's SPECS mission are introduced and asymptotic tracking laws based on output-feedback control are developed. The simulation results show that triangular system is superior in terms of parameter estimation compared to the more complex TetraStar formation, which is mainly due to the fact that we require the outer spacecraft of TetraStar to be uncontrolled, which renders the satellite formation uncontrollable and unstabilizable in general. From a controls point of view, TetraStar shows significant benefits. The control effort in radial direction for TetraStar becomes negligible; in angular direction we obtain a significant decrease in overall control impulse by requiring that the system angular momentum at $t = t_i$ and $t = t_f$ are equal. Even though this approach proves to be a reasonable technique of choosing the mass of the outer spacecraft, a better way of dramatically decreasing the overall control effort is to allow the outer tethers to be deployable and to use a tether deployment (retrieval) strategy that renders the angular momentum of the TSS virtually constant. As a final remark, we point out that the lack of control authority for the TetraStar configuration with uncontrollable counterweights turns out to be immaterial for in-plane maneuvers. The uncontrollability of the system greatly affects, however, plane changes such as retargeting maneuvers, which are certainly infeasible without the use of thrusters.

Acknowledgments

This work was supported by David Quinn of NASA Goddard Space Flight Center and by Arje Nachman of the U.S. Air Force Office of Scientific Research. The authors thank the Associate Editor and anonymous reviewers for their many helpful comments.

References

[1] Johnson, L., Glichrist, B., Estes, R. D., and Lorenzini, E., "Overview of Future NASA Tether Applications," *Advances in Space Research*, Vol. 24, No. 4, 1999, pp. 1055–1063.

[2] Maccone, C., "Tethered System to Get Magnified Radio Pictures of the Galactic Center from a Distance of 550 AU," *Acta Astronautica*, Vol. 45, No. 2, 1999, pp. 109–114.

[3] Quadrelli, M. B., Hadaegh, F. Y., Lorenzini, E. C., and Bombardelli, C., "Precision Tethered Formations for LEO and Space Interferometry Applications," DECANSO Paper 112, Dec. 2001.

[4] Hacker, B. C., and Grimwood, J. M., "On the Shoulders of Titans: A History of Project Gemini," NASA, Tech. Rept. SP-4203, 1977.

[5] Cosmo, M., and Lorenzini, E., *Tethers in Space Handbook*, 3rd ed., prepared for NASA/MSFC by Smithsonian Astrophysical Observatory, Cambridge, MA, 1997.

[6] Beletsky, V. V., and Levin, E. M., *Dynamics of Space Tether Systems*, Vol. 83, Advances in Astronautical Sciences, Univelt, San Diego, CA, 1993.

[7] Farley, R. E., and Quinn, D. A., "Tethered Formation Configurations—Meeting the Scientific Objectives of Large Aperture and Interferometric Science," AIAA Paper 2001-4770, 2001.

[8] Quinn, D. A., and Folta, D. C., "A Tethered Formation Flying Concept for the SPECS Mission," *Proceedings of the 23rd Rocky Mountain Guidance and Control Conference*, Vol. 104, Advances in the Astronautical Sciences, Univelt Inc. Publishers, San Diego, CA, 2000, pp. 183–196.

[9] Decou, A. B., "Tether Static Shape for Rotating Multimass, Multitether, Spacecraft for Triangle Michelson Interferometer," *Journal of Guidance and Control*, Vol. 12, No. 2, March–April 1989, pp. 273–275.

[10] Decou, A. B., "Attitude and Tether Vibration Control in Spinning Tethered Triangles for Orbiting Interferometry," *Journal of the Astronautical Sciences*, Vol. 41, No. 3, July–Sept. 1993, pp. 373–398.

[11] Keshmiri, M., and Misra, A. K., "General Formulation for N-body Tethered Satellite System Dynamics," *Journal of Guidance, Control, and Dynamics*, Vol. 19, No. 1, Jan.–Feb. 1996, pp. 75–83.

[12] Wong, B., and Misra, A. K., "Dynamics of a Tethered System near the Earth-Moon Lagrangian Points," *Proceedings of the 2003 AAS/AIAA Space Flight Mechanics Meeting*, Vol. 114, Advances in the Astronautical Sciences, Univelt Inc. Publishers, San Diego, CA, 2003, pp. 1675–1694.

[13] Farquhar, R. W., "Tether Stabilization at a Collinear Libration Point," *Journal of the Astronautical Sciences*, Vol. 49, No. 1, Jan.–March 2001, pp. 91–106.

[14] Kim, M., and Hall, C. D., "Control of a Rotating Variable-Length Tethered System," *Journal of Guidance, Control, and Dynamics*, Vol. 27, No. 5, 2004, pp. 849–858.

[15] Marino, R., and Tomei, P., "Global Adaptive Output-Feedback Control of Nonlinear Systems, Part 1: Linear Parametrization," *IEEE Transactions on Automatic Control*, Vol. 38, No. 1, Jan. 1993, pp. 17–32.

[16] Marino, R., and Tomei, P., "Global Adaptive Output-Feedback Control of Nonlinear Systems, Part 2: Nonlinear Parametrization," *IEEE Transactions on Automatic Control*, Vol. 38, No. 1, Jan. 1993, pp. 33–48.

[17] Marino, R., and Tomei, P., "An Adaptive Output Feedback Control for a Class of Nonlinear Systems with Time-Varying Parameters," *IEEE Transactions on Automatic Control*, Vol. 44, No. 11, Nov. 1999, pp. 2190–2194.

[18] Krstić, M., and Kokotović, P., "Adaptive Nonlinear Output-Feedback Schemes with Marino-Tomei Controller," *IEEE Transactions on Automatic Control*, Vol. 41, No. 2, Feb. 1996, pp. 274–280.

[19] Khalil, H. K., "Adaptive Output Feedback Control of Nonlinear Systems Represented by Input-Output Models," *IEEE Transactions on Automatic Control*, Vol. 41, No. 2, Feb. 1996, pp. 177–188.

[20] Loria, A., "Global Tracking Control of One Degree of Freedom Euler-Larange Systems with Velocity Measurements," *European Journal of Control*, Vol. 2, No. 2, June 1996, pp. 144–151.

[21] de Queiroz, M. S., Dawson, D. M., Nagarkatti, S. P., and Zhang, F., *Lyapunov-Based Control of Mechanical Systems, Control Engineering*, Birkhäuser Boston, Cambridge, MA, 2000.

[22] Kim, M., and Hall, C. D., "Lyapunov and Halo Orbits About L_2," *Proceedings of the 2001 AAS/AIAA Astrodynamics Specialist Conference*, Vol. 109, Advances in the Astronautical Sciences, Univelt Inc. Publishers, San Diego, CA, 2002, pp. 349–366.

[23] Gates, S. S., "Multi-Tethered Space-Based Interferometers: Particle System Model," Naval Research Laboratory, Tech. Rept. NRL/MR/8231-01-8579, Washington, D.C., Sept. 2001.

[24] Nicosia, S., and Tomei, P., "Robot Control by Using Only Joint Position Measurements," *IEEE Transactions on Automatic Control*, Vol. 35, No. 9, Sept. 1990, pp. 1058–1061.

C. McLaughlin
Associate Editor